



# Radiative Effects on the Formation of the Stably Stratified Layer in the Lower Atmosphere of Venus

Takahashi, Yoshiyuki O. ; Hayashi, Yoshi-Yuki ; Hashimoto, George L. ; Kuramoto, Kiyoshi ; Ishiwatari, Masaki ; Kashimura, Hiroki

---

**(Citation)**

Journal of the Meteorological Society of Japan. Ser. II, 102(5):469-483

**(Issue Date)**

2024

**(Resource Type)**

journal article

**(Version)**

Version of Record

**(Rights)**

© The Author(s) 2024.

This is an open access article published by the Meteorological Society of Japan under a Creative Commons Attribution 4.0 International (CC BY 4.0) license.

**(URL)**

<https://hdl.handle.net/20.500.14094/0100490447>



## Radiative Effects on the Formation of the Stably Stratified Layer in the Lower Atmosphere of Venus

Yoshiyuki O. TAKAHASHI, Yoshi-Yuki HAYASHI

*Department of Planetology, Kobe University, Kobe, Japan  
Center for Planetary Science, Kobe University, Kobe, Japan*

George L. HASHIMOTO

*Department of Earth Sciences, Okayama University, Okayama, Japan*

Kiyoshi KURAMOTO, Masaki ISHIWATARI

*Department of Cosmo sciences, Hokkaido University, Hokkaido, Japan*

and

Hiroki KASHIMURA

*Department of Planetology, Kobe University, Kobe, Japan  
Center for Planetary Science, Kobe University, Kobe, Japan*

*(Manuscript received 17 January 2024, in final form 7 May 2024)*

### Abstract

The formation of the stable layer below about  $2 \times 10^6$  Pa pressure level (about 20 km altitude) of the atmosphere of Venus detected by in situ observations is investigated by the use of a radiative-convective equilibrium model. We demonstrate that, assuming mixing ratio profiles of absorbers to be at the upper limits of the observed ranges for H<sub>2</sub>O and SO<sub>2</sub> and the lower limit for CO, a stable layer forms as a radiative-convective equilibrium state, but its stability is lower than the observed one. Also, increasing the continuum absorption coefficient of CO<sub>2</sub> and/or H<sub>2</sub>O, which are not well constrained observationally or experimentally, results in the formation of a stable layer whose stability is comparable to the observed one. These results suggest a practical method to form the stable layer in the dynamical models of the Venus atmosphere. Further, these results indicate that the important targets of future observations and laboratory measurements are to obtain more precise profiles of the mixing ratios of H<sub>2</sub>O, CO, and SO<sub>2</sub> in the Venus atmosphere, and to determine the continuum absorption coefficients of those.

**Keywords** Venus lower atmosphere; stable layer below clouds; radiative-convective equilibrium; continuum absorption

**Citation** Takahashi, Y. O., Y.-Y. Hayashi, G. L. Hashimoto, K. Kuramoto, M. Ishiwatari, and H. Kashimura, 2024: Radiative effects on the formation of the stably stratified layer in the lower atmosphere of Venus. *J. Meteor. Soc. Japan*, **102**, 469–483, doi:10.2151/jmsj.2024-025.

---

Corresponding author: Yoshiyuki O. Takahashi, Department of Planetology, Kobe University, 1-1, Rokkodaicho, Nada-ku, Kobe 657-8501, Japan  
E-mail: yot@gfd-dennou.org  
J-stage Advance Published Date: 23 May 2024



## 1. Introduction

The structure of the lower atmosphere of Venus, below the cloud layer around 50 km to 70 km, has not been understood well due to the existence of the globally-covering thick cloud layer. In situ observations of the Venera probes, the Pioneer Venus probes, and the VEGA-2 lander indicated that the atmosphere below the cloud layer was generally statically stable except for several altitude regions. One of the peculiar features of the lower atmosphere of Venus is the existence of a stable layer below about 20 km altitude ( $\sim 2 \times 10^6$  Pa pressure level).

The observed stability of the lower atmosphere of Venus varies with altitude. The atmospheric layer is stable just below the cloud base down to about 30 km altitude ( $\sim 1 \times 10^6$  Pa), close to neutral around 20–30 km altitude ( $\sim 2 \times 10^6$ – $1 \times 10^6$  Pa), stable from about 20 km to at least about 12 km altitude ( $\sim 4 \times 10^6$  Pa) where the Pioneer Venus probe sounding ended (Seiff 1983) or to about 6.5 km altitude ( $\sim 6 \times 10^6$  Pa) based on the VEGA-2 lander observation (Seiff and the VEGA Balloon Science Team 1987), and suggested to be unstable further below down to the surface. The layer close to statically neutral around 20–30 km altitude ( $\sim 2 \times 10^6$ – $1 \times 10^6$  Pa) was observed to have variability in its depth by the Pioneer Venus probes and the VEGA-2 lander (Seiff 1983; Seiff and the VEGA Balloon Science Team 1987), but the neutral layer was detected by all observations.

The neutral layer would be produced by “convection” which includes the small scale one, such as that shown by numerical simulations (e.g., Baker et al. 2000a, b), and the large scale circulation. The existence of the unstable layer close to the surface is curious, since it should be neutralized by “convection.” Compositional separation is suggested as a mechanism to stabilize the thermal instability of the layer (Lebonnois and Schubert 2017).

As for the stable layer below about 20 km altitude ( $\sim 2 \times 10^6$  Pa), it is not a regional or temporal one which is produced dynamically, but is a global and persistent one. It has been observed by the Venera 10–12 probes, four Pioneer Venus probes, and the VEGA-2 lander, over wide range of local time from 0:07 to 13:45 and latitude from 31.2°S to 59.3°N.

The stable layer in the lower atmosphere of Venus should have a large influence on the vertical transport of minor constituents and angular momentum, since convection is suppressed in the stable layer. The stable layer may play an important role even in the generation of superrotation by suppressing the

vertical mixing, since a small vertical eddy viscosity is required to generate fast superrotation in General Circulation Model (GCM) experiments (Sugimoto et al. 2019).

A number of numerical studies have been performed to investigate the structure of the lower atmosphere of Venus by the use of one-dimensional radiative-convective equilibrium models (Pollack and Young 1975; Matsuda and Matsuno 1978; Takagi et al. 2010; Ikeda 2011; Lee and Richardson 2011; Lebonnois et al. 2015; Mendonça et al. 2015; Takahashi et al. 2024) and GCMs (e.g., Lebonnois et al. 2018). However, most of these studies treated the Venus atmosphere as an ideal gas, and the stability could not be calculated accurately in those studies. Among them, Takahashi et al. (2024) treated the Venus atmosphere as a mixture of real gases by the use of the thermodynamic properties derived from the EOS-CG mixture model (EOS-CG: Equation of State for Combustion Gases and Combustion Gas-like Mixtures) (Gernert and Span 2016), which describes the reduced Helmholtz energy of real gas mixture. However, the stable layer below about 20 km altitude ( $\sim 2 \times 10^6$  Pa) was not represented in the radiative-convective equilibrium presented by Takahashi et al. (2024).

In this study, the formation of the stable layer below about  $2 \times 10^6$  Pa pressure level ( $\sim 20$  km altitude) in the atmosphere of Venus is investigated by the use of a one-dimensional radiative-convective equilibrium model with the thermodynamic property of the real gas. We do not step into the possibility of compositional separation suggested by Lebonnois and Schubert (2017), but try to examine the thermal structure of the atmosphere under the assumption of constant mean molecular weight. We focus on the vertical thermal structure in the global mean sense in this study, though recent studies by the use of GCMs have shown the presence of a large scale activity in the Venus lower atmosphere (e.g., Lebonnois et al. 2016; Sugimoto et al. 2019). The use of the one-dimensional model is appropriate since the lower atmosphere of Venus is horizontally nearly uniform, e.g., the difference in temperature observed by four Pioneer Venus probes is a few kelvins in the lower atmosphere (Seiff et al. 1980), and that indicated by Galileo NIMS is no more than  $\pm 2$  K (Hashimoto et al. 2008).

In the followings, the radiative-convective equilibrium model for Venus atmosphere used in this study is described in Section 2. The experimental setup for the control experiment, which reproduces the radiative-convective equilibrium by Takahashi et al. (2024), is also described, there. In Section 3, the equilibrium

structure of the control experiment is described along with the characteristics of its radiative temperature tendency spectra. The sensitivity experiments are performed to investigate whether the stable layer forms or not in the cases with the different cloud settings, the different radiatively active gas distributions, and the increased intensities of continuum absorption of gases in Section 4. Implications of the results are discussed in Section 5. Finally, conclusions of this study are presented in Section 6.

## 2. Model and experimental setup

We use the radiative-convective equilibrium model developed by Takahashi et al. (2024) with  $k$ -distribution tables newly generated in this study. Radiative-convective equilibrium is obtained by integrating time evolution equations for energies of atmosphere and a uniform slab at the surface. In atmospheric energy calculation, thermodynamic variables are evaluated for a mixture of real gases composed of 96.5 % CO<sub>2</sub> and 3.5 % N<sub>2</sub> (von Zahn et al. 1983) by the use of the EOS-CG mixture model (Gernert and Span 2016). The dry convective adjustment is applied when the lapse rate is greater than the dry adiabatic lapse rate. In addition, surface temperature is assumed to be the same as atmospheric temperature just above the surface.

The radiative fluxes are calculated by the use of the correlated  $k$ -distribution radiation model of Takahashi et al. (2023). In this study, the  $k$ -distribution tables used in this radiation model were newly generated from the results of our line-by-line model (Takahashi et al. 2023) to perform parameter experiments with a variety of profiles of radiatively active gases and particles, and with different intensities of continuum absorption of gases. The details of the line-by-line model and optical parameters, such as a molecular absorption database, a line shape function, continuum absorption coefficients, and the solar insolation spectrum, used to generate the  $k$ -distribution table are described by Takahashi et al. (2023), and the specification of the newly generated table can be found in Appendix A.

In the correlated  $k$ -distribution radiation model, the radiative transfer equation with the generalized two-stream approximation (Meador and Weaver 1980) is solved with the method of Toon et al. (1989). In calculating radiative fluxes, absorption and Rayleigh scattering by gases, and absorption and scattering by particles are taken into account. Radiatively active gas components considered in radiation calculations are H<sub>2</sub>O, CO<sub>2</sub>, CO, SO<sub>2</sub>, HF, OCS, and N<sub>2</sub>. As for the particles, radiatively active cloud particles referred to as modes 1, 2, 2', and 3, which have different radii

(Esposito et al. 1983; Ragent et al. 1985), are considered. In addition, “unknown ultraviolet (UV) absorber,” which contributes almost the half of absorption of solar radiation (Crisp 1986), is also included.

We take into account continuum absorptions of the CO<sub>2</sub>–CO<sub>2</sub> collision induced absorption, hereafter referred to as CO<sub>2</sub> continuum absorption, and the H<sub>2</sub>O continuum absorption. The coefficient for CO<sub>2</sub> continuum absorption is obtained from several sources (Takahashi et al. 2023). For temperatures outside of the temperature range of the data, the values at the closest temperature in the data are used. The coefficient for H<sub>2</sub>O continuum absorption is obtained from the version 3.0 of the MT\_CKD model, which is the empirical model of the continuum absorption for the Earth’s atmosphere [the description on version 2.5 of the MT\_CKD model is given by Mlawer et al. (2012)].

The atmospheric energy equation is discretized and radiative-convective equilibrium calculations are performed with 80 atmospheric layers (81 levels) based on the VIRA (Venus International Reference Atmosphere) model (Seiff et al. 1985). Initial condition is the low latitude temperature profile of the VIRA model. In time integration, profiles of atmospheric compositions, the clouds, and the UV absorber are fixed. The incident solar radiation flux at the top of the atmosphere is assumed to be 2635 W m<sup>−2</sup>. The surface albedo is set to 0.05 in wavenumber larger than 7700 cm<sup>−1</sup>, and is zero in smaller wavenumber range. In order to evaluate the global mean of solar radiation, radiative fluxes are calculated at two solar zenith angles of 37.9° and 77.8°, are averaged, and halved considering no solar flux at night (Takahashi et al. 2023).

The control experiment is performed with profiles of the radiatively active gases based on Pollack et al. (1993) (Fig. 1a), and the clouds and the UV absorber based on Crisp (1986) (Fig. 1b) in radiation calculation.

## 3. Radiative-convective equilibrium of the control experiment

The radiative-convective equilibrium profile of the control experiment is shown in Fig. 2. There is a stable layer around  $6 \times 10^5$ – $2 \times 10^5$  Pa pressure levels similarly to the VIRA model. Below the layer down to the surface, the atmosphere is statically neutral unlike the VIRA model in which there is the stable layer below about  $2 \times 10^6$  Pa pressure level. These characteristics are the same as those observed in the radiative-convective equilibrium profile under the same condition shown by Takahashi et al. (2024).

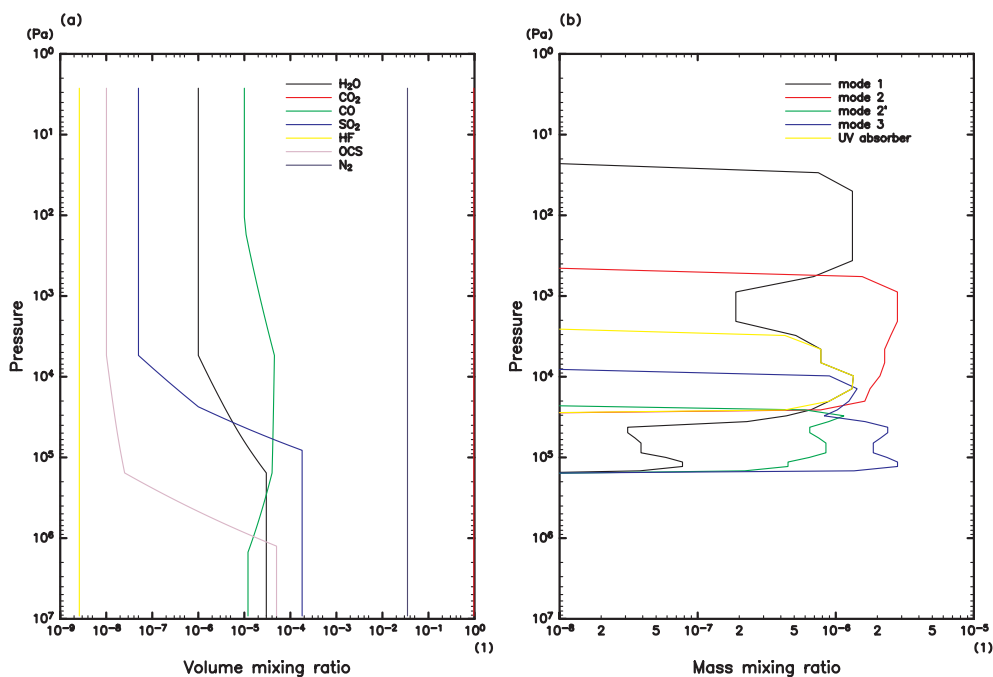


Fig. 1. Vertical profiles of volume mixing ratios of gases and mass mixing ratios of clouds and UV absorber used in the control experiment: profiles of (a) gases and (b) clouds and UV absorber.

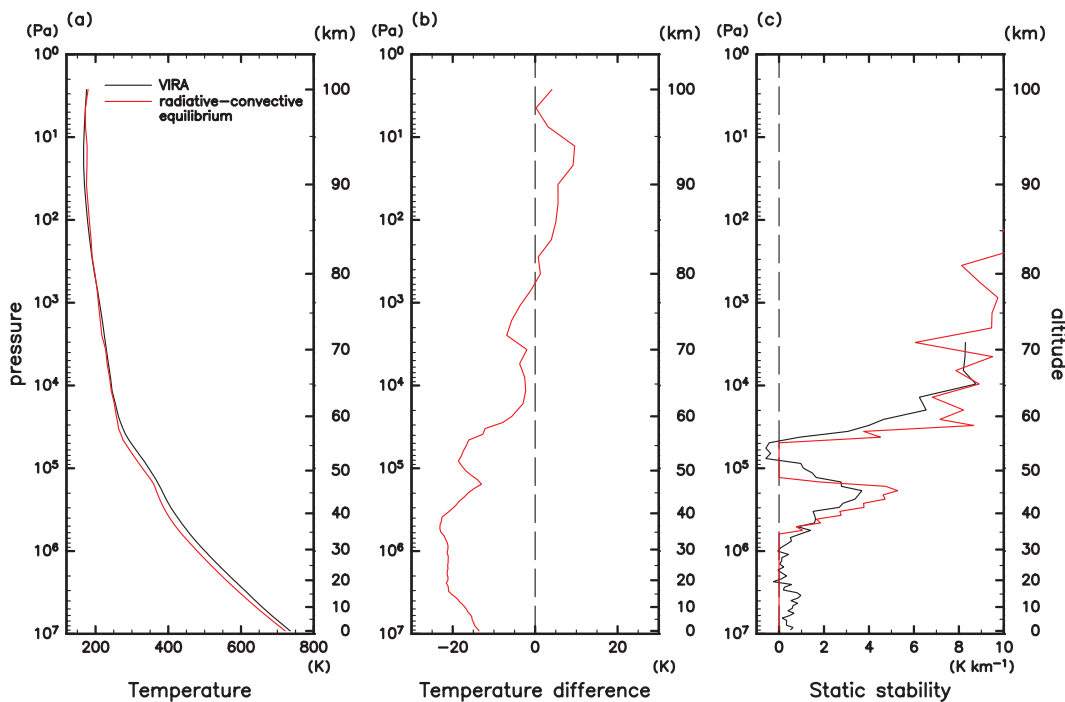


Fig. 2. Radiative-convective equilibrium profiles of (a) temperature, (b) temperature difference from the low latitude profile of the VIR model, and (c) static stability for the control experiment (red). The black lines are those of the low latitude profiles of the VIR model.

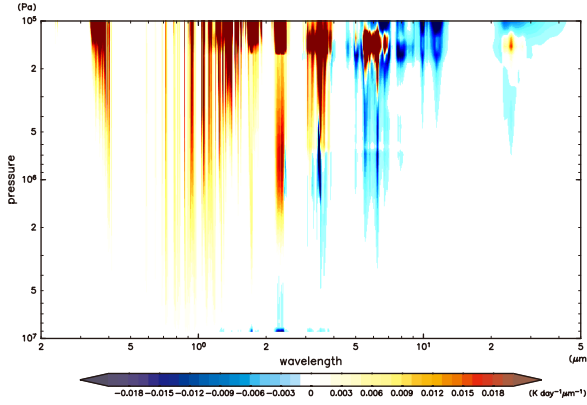


Fig. 3. Radiative temperature tendency spectrum (Eq. 1) for the radiative-convective equilibrium of the control experiment below  $1 \times 10^5$  Pa pressure level. Plotted are the running averaged values with the interval of  $15 \text{ cm}^{-1}$ .

In order to diagnose the radiative effects of the clouds, the UV absorber, and each gas component on the stability in the lower atmosphere, we calculated the radiative temperature tendency spectra and its sensitivity to opacity changes for the radiative-convective equilibrium profile of the control experiment by the use of our line-by-line model (Takahashi et al. 2023). The radiative temperature tendency spectrum is expressed as follows:

$$Q_{\text{rad}}(p, \lambda; \tau_{\text{ptcl}}, \tau_{\text{gas}}) = \frac{g}{C_p(p, T(p))} \frac{\partial F_{\text{net}}(p, \lambda; \tau_{\text{ptcl}}, \tau_{\text{gas}})}{\partial p}, \quad (1)$$

where  $p$ ,  $T$ ,  $\lambda$ ,  $g$ ,  $C_p$ ,  $F_{\text{net}}$  are pressure, temperature, wavelength, the gravitational acceleration, the specific heat at constant pressure, and the net radiative flux, respectively. Note that  $\tau_{\text{ptcl}}$  and  $\tau_{\text{gas}}$  are the optical depths of the clouds and the UV absorber, and the optical depth of gases, respectively. These optical depths are actually given as functions of pressure and wavelength, but are expressed symbolically here.

The radiative temperature tendency spectrum in the lower atmosphere is shown in Fig. 3, and that up to the top of the model is shown in Fig. B1 in Appendix B for reference. Radiative temperature tendency in wavelengths shorter than  $1 \mu\text{m}$  is positive over the whole altitudes, and that in wavelengths from  $1 \mu\text{m}$  to  $2 \mu\text{m}$  is negative just above the surface, and is positive above there. The negative tendency region extends to about  $3 \times 10^6$ ,  $7 \times 10^5$  and  $2 \times 10^5$  Pa pressure levels around  $2.4$ ,  $3\text{--}4$  and  $5\text{--}7 \mu\text{m}$ , respectively.

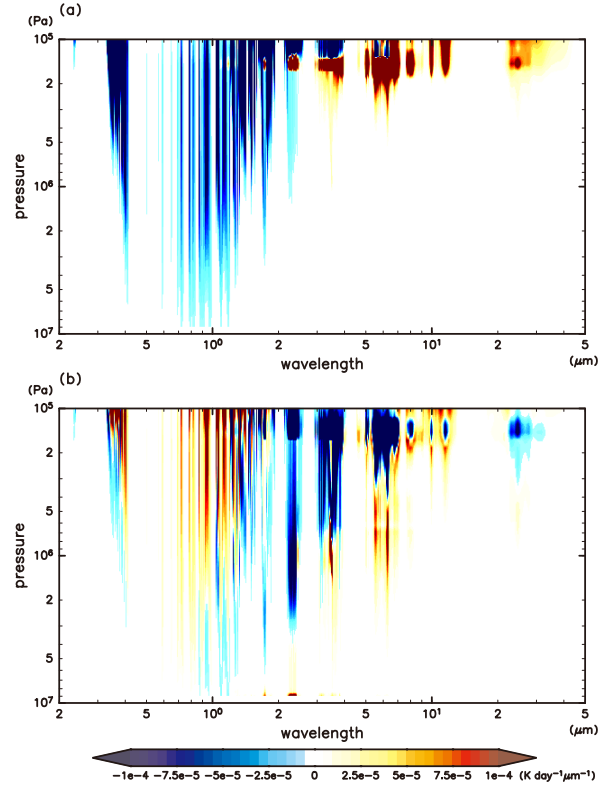


Fig. 4. Changes in radiative temperature tendency spectra from that of the control experiment: (a) the change when the optical depths due to the clouds and the UV absorber are increased by 1 % (Eq. 2) and (b) that when the optical depth of gas absorption are increased by 1 % (Eq. 3). Plotted are the running averaged values with the interval of  $15 \text{ cm}^{-1}$ .

The temperature as high as about 700 K in the lower atmosphere of Venus, the surface temperature same as atmospheric temperature just above the surface, and the vertical profile of optical depth cause the effective radiative cooling near the surface in several near infrared wavelengths.

Figure 4 shows the changes in the radiative temperature tendency spectra when the optical depths of the clouds and the UV absorber are increased by 1 %, namely,

$$\Delta Q_{\text{rad, ptcl}}(p, \lambda) = Q_{\text{rad}}(p, \lambda; \tau_{\text{ptcl}} \times 1.01, \tau_{\text{gas}}) - Q_{\text{rad}}(p, \lambda; \tau_{\text{ptcl}}, \tau_{\text{gas}}), \quad (2)$$

and when the optical depth of gas absorption is increased by 1 %, namely,



$$\Delta Q_{rad,gas}(p,\lambda) = Q_{rad}(p,\lambda;\tau_{ptcl},\tau_{gas}\times 1.01) - Q_{rad}(p,\lambda;\tau_{ptcl},\tau_{gas}). \quad (3)$$

Figure 4a shows that the vertical gradient of the change in the radiative temperature tendency due to the increase in optical depths of the clouds and the UV absorber is negative around 0.3–3  $\mu\text{m}$ . The vertical gradient is caused by the fact that the solar heating is larger at high levels than that at low levels. For wavelengths longer than 3  $\mu\text{m}$ , the radiative temperature tendency in the cloud layer above about  $2 \times 10^5$  Pa pressure level is increased at several wavelengths, but that is small below there. These imply that the increase in the optical depths of the clouds and the UV absorber tends to destabilize the atmosphere below about  $2 \times 10^5$  Pa pressure level. On the contrary, the increase in the optical depths of the clouds and the UV absorber decreases the downward solar radiation flux integrated over wavelength at the surface (not shown in the figure). This tends to stabilize the atmosphere just above the surface.

Figure 4b shows that the effect of the increase in the optical depth of gas absorption on the static stability of the atmosphere depends on wavelength and pressure. The increase in the optical depth of gas which absorbs the radiation around 1  $\mu\text{m}$  tends to stabilize the atmospheric layer between the surface and the cloud base, since the vertical gradient of the change in the radiative temperature tendency is positive. The increase in the optical depth of gas which absorbs the radiation around 3–4  $\mu\text{m}$  and 5–7  $\mu\text{m}$  will stabilize the atmospheric layer below the  $2 \times 10^6$  Pa pressure level, since the vertical gradient of the change in the radiative temperature tendency is positive. Also, the increase in the optical depth of gas which absorbs the radiation around 1.6–2.4  $\mu\text{m}$  tends to destabilize the lower atmosphere due to the increased heating close to the surface and the increased cooling above about  $5 \times 10^6$  Pa pressure level. These imply that the increase in the mixing ratios of  $\text{H}_2\text{O}$  and  $\text{SO}_2$  increases the stability, while the increase in the optical depth of CO decreases the stability, since absorption by  $\text{SO}_2$ ,  $\text{H}_2\text{O}$ , and CO are dominant around 4 and 7, 5–7, and 2.4  $\mu\text{m}$ , respectively (Fig. 5).

#### 4. Sensitivity of the formation of the stable layer

We examined the sensitivity of the formation of the stable layer below about  $2 \times 10^6$  Pa pressure level ( $\sim 20$  km altitude) to the mixing ratios of the clouds and the UV absorber, the mixing ratios of radiatively active gases, and the intensities of continuum absorp-

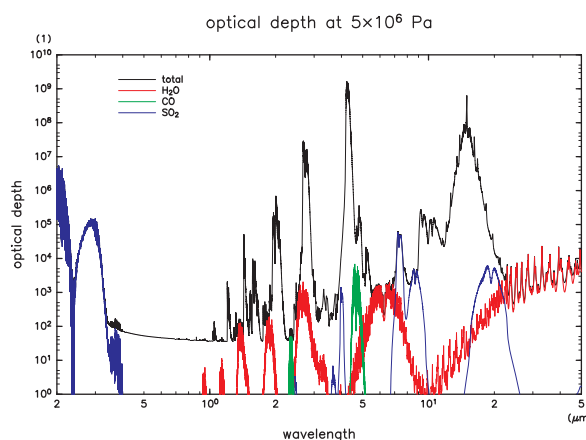


Fig. 5. Spectra of optical depth at  $5 \times 10^6$  Pa pressure level for the low latitude temperature profile of the VIRa model. The black, red, green and blue lines show optical depths of the total extinction,  $\text{H}_2\text{O}$ , CO, and  $\text{SO}_2$  absorption, respectively.

tion of gases. As shown in the previous section, the optical depths of the clouds and the UV absorber, and the optical depth of gas are able to affect the stability of the lower atmosphere of Venus.

Also, we evaluated whether an increase in the intensity of continuum absorption in 3–7  $\mu\text{m}$  contributed to the formation of the stable layer. For the climate studies of the Earth, the intensity of continuum absorption has usually been given by an empirical model, such as the MT\_CKD model (Mlawer et al. 2012). However, the intensity of the continuum absorption is very uncertain under the condition of the Venus lower atmosphere, which is very different from that of the Earth's atmosphere. Thus, the intensity of continuum absorption is sometimes used as a tunable parameter to obtain the radiative fields consistent with observations (e.g., Eymet et al. 2009). In this study, we varied the absorption coefficient in the range of 3–7  $\mu\text{m}$ , though the formation of the stable layer is probably affected by the opacity of the spectral range of 1–7  $\mu\text{m}$  (Section 3). We did not modify the absorption coefficient in the range of 1–2  $\mu\text{m}$ , since it is constrained by the ground-based and the spacecraft observations of the thermal emission from the Venus deep atmosphere (e.g., Allen and Crawford 1984; Titov et al. 2007).

It may be worth mentioning that there is the presence of hazes below the clouds down to about 30 km altitude (e.g., Esposito et al. 1983). However, it is unlikely that the haze has a significant effect on the thermal structure since its number density is small.

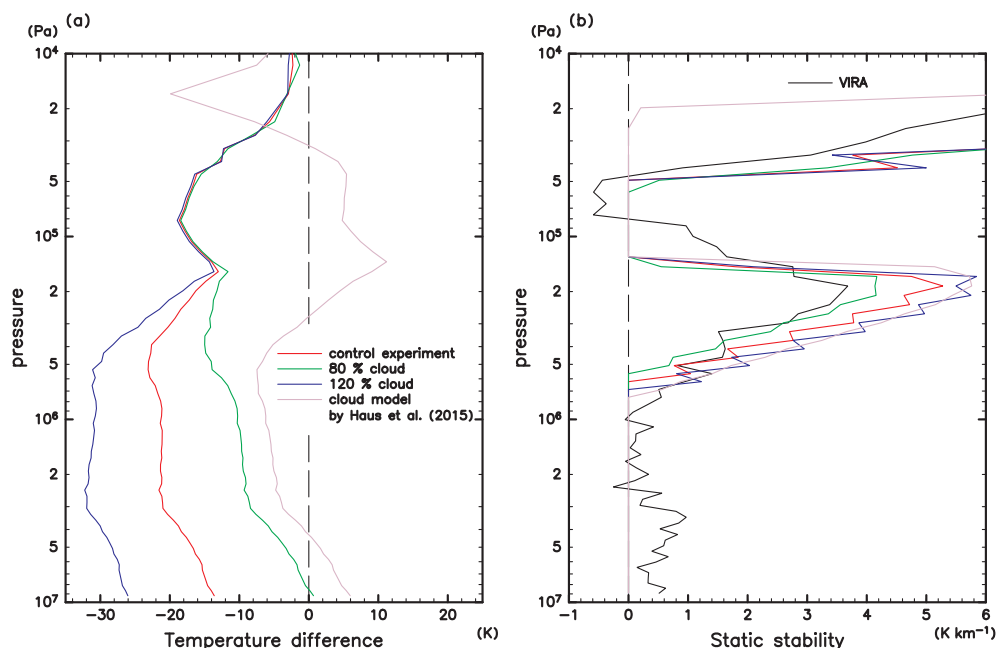


Fig. 6. Radiative-convective equilibrium profiles of (a) temperature difference from the low latitude profile of the VIRA model, and (b) static stability. The green and blue lines show the profiles calculated with the mixing ratios decreased to 80 % and increased to 120 % for both of the clouds and the UV absorber from the control experiment, respectively. The magenta lines show those calculated with the cloud model by Haus et al. (2015). The red and black lines are those of the control experiment and the low latitude profile of the VIRA model, respectively.

#### 4.1 Sensitivity to cloud settings

Figure 6 shows the radiative-convective equilibrium profiles calculated with the mixing ratios decreased to 80 % and increased to 120 % for both of the clouds and the UV absorber from the control experiment. It is shown that the atmosphere is statically neutral below about  $8 \times 10^5$  Pa pressure level in both cases, though the thickness of the neutral layer is smaller in the latter case reflecting smaller downward solar radiation flux at the surface. It is worth mentioning that the stable layer does not form even in the cases with the further decreased and the further increased mixing ratios for both of the clouds and the UV absorber from the control experiment (figure is not shown).

In Fig. 6, the radiative-convective equilibrium profiles calculated with the cloud model of Haus et al. (2015) are also shown to examine the dependence of stable layer formation on the formulation of cloud model. The stable layer does not form in this case, either. The cloud model of Haus et al. (2015) is based on the remote sensing observations by the Venus Express (see Appendix C for the details of the adopted cloud model), and is somewhat different from the cloud model of our control experiment adopted from

Crisp (1986, 1989) based on the in situ and remote sensing observations by the Pioneer Venus probes and orbiter. Our results suggest that, under the atmospheric gas radiation properties of the control experiment, the stable layer does not form independent of the details of the cloud model.

#### 4.2 Sensitivity to gas distribution

The upper and the lower limit of  $\text{H}_2\text{O}$ ,  $\text{CO}$ , and  $\text{SO}_2$  mixing ratios inferred from various observations (Bertaux et al. 1996; Bézard et al. 1990, 1993; Connes et al. 1968; de Bergh et al. 1995; Gel'man et al. 1979; Hoffman et al. 1980a, b; Marcq et al. 2008; Marov et al. 1989; Moroz et al. 1979; Oyama et al. 1980; Pollack et al. 1993; Taylor et al. 1997; Tsang et al. 2009; von Zahn et al. 1983; Winick and Stewart 1980; Young 1972) compiled by Johnson and de Oliveira (2019) (Fig. 7) are used to examine the sensitivity of the formation of the stable layer. The stable layer below about  $2 \times 10^6$  Pa pressure level forms only in the case with the upper limit profiles of  $\text{H}_2\text{O}$  and  $\text{SO}_2$  and the lower limit profile of  $\text{CO}$  (Fig. 8). This is consistent with the results shown in Section 3. However, the stability of the stable layer is lower than that of the



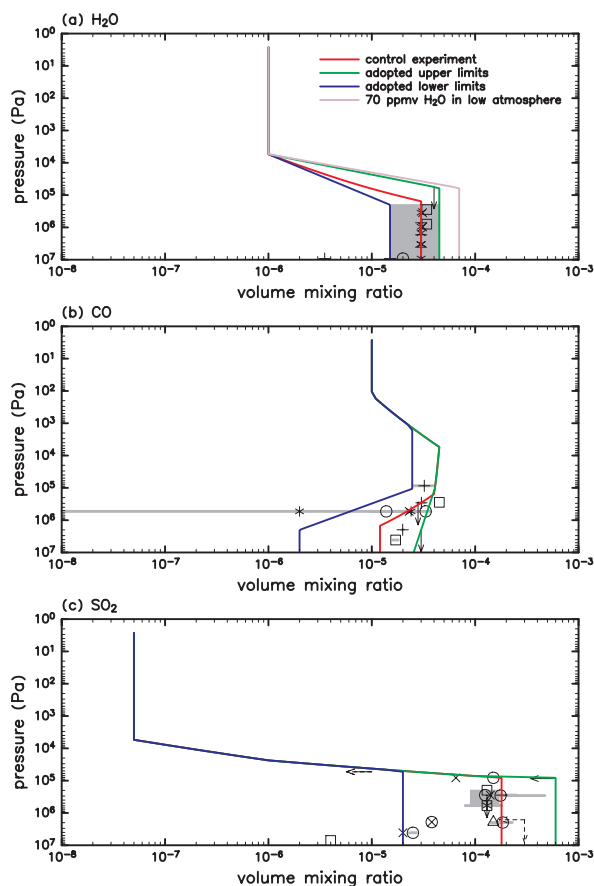


Fig. 7. Volume mixing ratios of (a)  $\text{H}_2\text{O}$ , (b)  $\text{CO}$ , and (c)  $\text{SO}_2$  used for the sensitivity experiment to the distribution of radiatively active gas. The red lines show the profiles for the control experiment. The green and blue lines show those adopted in the experiment as the upper and the lower limits of the observational variability and ambiguity, respectively. Also shown in panel (a) is the  $\text{H}_2\text{O}$  profile with the maximum volume mixing ratio of 70 ppmv in the lower atmosphere (magenta). In each panel, the observations compiled by Johnson and de Oliveira (2019), excluding potentially uncertain data, are plotted for the sake of comparison; marks, leftward arrows, and downward arrows indicate means, upper limits and uppermost heights of observational mixing ratios obtained by each instrument, respectively. Note that the tails of arrows represent the values of mixing ratio and height. The horizontal gray bars and gray tones indicate ranges of the reported observational errors.

VIRA model.

When the  $\text{H}_2\text{O}$  mixing ratio in the lower atmosphere is increased to 70 ppmv (Fig. 7a), the stability of the stable layer become comparable to that of the VIRA model (Fig. 8). However, the volume mixing ratio in this case is about double of the observed mean (30 ppmv) and is out of range of observed values. If one trusts the observed  $\text{H}_2\text{O}$  mixing ratio, then the stable layer cannot be formed by the radiative forcing of  $\text{H}_2\text{O}$ .

#### 4.3 Sensitivity to intensity of continuum absorption

Figure 9 shows the radiative-convective equilibrium profiles calculated with the coefficients of  $\text{CO}_2$  and  $\text{H}_2\text{O}$  continuum absorption increased by factors of 10, 30, and 50. In these calculations, the continuum absorption coefficient in the range of  $3\text{--}10\ \mu\text{m}$  ( $1000\text{--}3500\ \text{cm}^{-1}$ ) was increased by multiplying constant factors independent of the temperature and pressure. The range of factors from 10 to 50 is chosen since the dependence of the stability around  $8 \times 10^6\text{--}3 \times 10^6\ \text{Pa}$  pressure levels on the factor can be observed clearly. In addition, the range encompasses the factor of 30 which will be determined for the coefficient of  $\text{CO}_2$  continuum absorption by a least squares method to fit the equilibrium temperature to the temperature of the VIRA model in Section 5.

When the coefficient for  $\text{CO}_2$  or  $\text{H}_2\text{O}$  continuum absorption is increased by a factor of more than 30, the stable layer forms around  $8 \times 10^6\text{--}3 \times 10^6\ \text{Pa}$  pressure levels. The larger the absorption coefficient is, the more stable the layer is. On the one hand, when the absorption coefficient is increased, the surface temperature is higher than observed one, e.g., 735 K observed by Venera 12 (Avduevskiy et al. 1983), due to the increased optical depth.

## 5. Discussion

It has been shown that the stable layer forms below about  $2 \times 10^6\ \text{Pa}$  pressure level when the coefficient for  $\text{CO}_2$  continuum absorption or  $\text{H}_2\text{O}$  continuum absorption is increased. However, in both cases, the surface temperature is higher than observed one. The surface temperature should decrease when the mixing ratios of the clouds and the UV absorber were increased (Fig. 6).

Actually, we found some pairs of the continuum absorption coefficient and the mixing ratios of the clouds and the UV absorber which led to the equilibrium temperature profile in which surface temperature as well as the stability of the stable layer close to those of the VIRA model by the use of a least squares

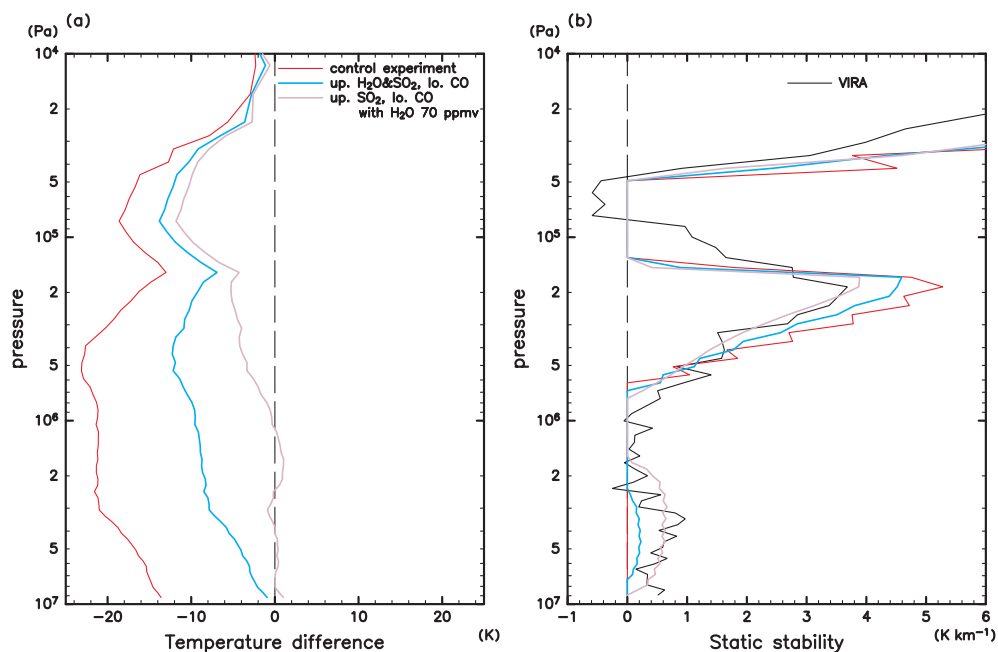


Fig. 8. Same as Fig. 6, but for the sensitivity experiment to the distribution of radiatively active gas. The cyan lines show the profiles calculated with the upper limit profiles of  $\text{H}_2\text{O}$  and  $\text{SO}_2$  and the lower limit profile of  $\text{CO}$  shown in Fig. 7. The magenta lines show those calculated with the upper limit profile of  $\text{SO}_2$ , the lower limit profile of  $\text{CO}$ , and the profile of  $\text{H}_2\text{O}$  with the maximum mixing ratio of 70 ppmv in the lower atmosphere.

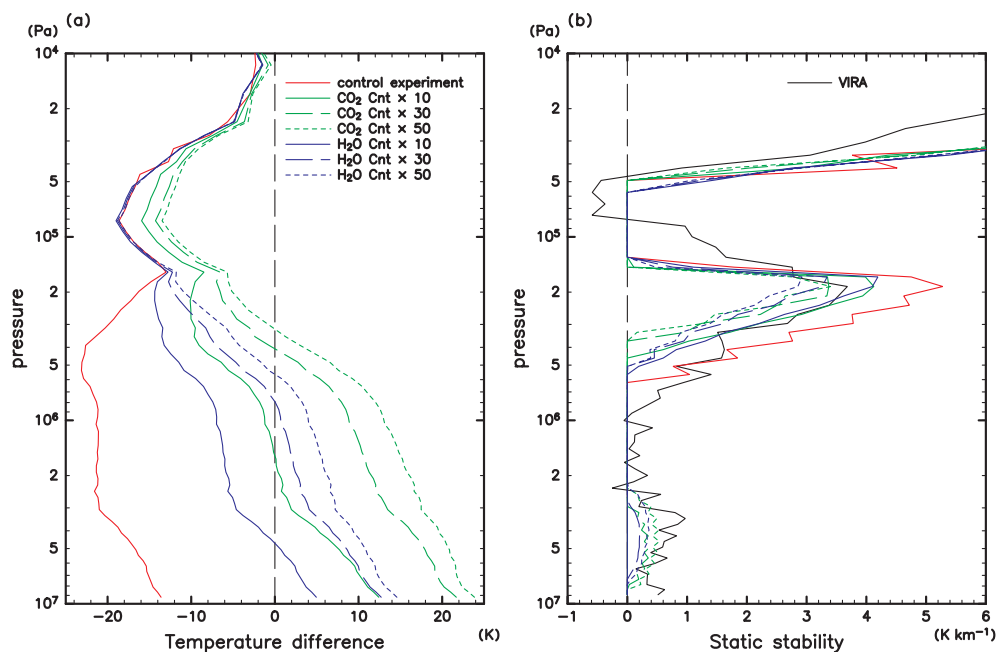


Fig. 9. Same as Fig. 6, but for the sensitivity experiments to the intensities of the  $\text{CO}_2$  and  $\text{H}_2\text{O}$  continuum absorption coefficients in 3–10  $\mu\text{m}$ . The green solid, dashed, and dotted lines show profiles calculated with the  $\text{CO}_2$  absorption coefficient increased by factors of 10, 30, and 50, respectively. Those blue lines are the same as green lines, but for the increased  $\text{H}_2\text{O}$  absorption coefficient.

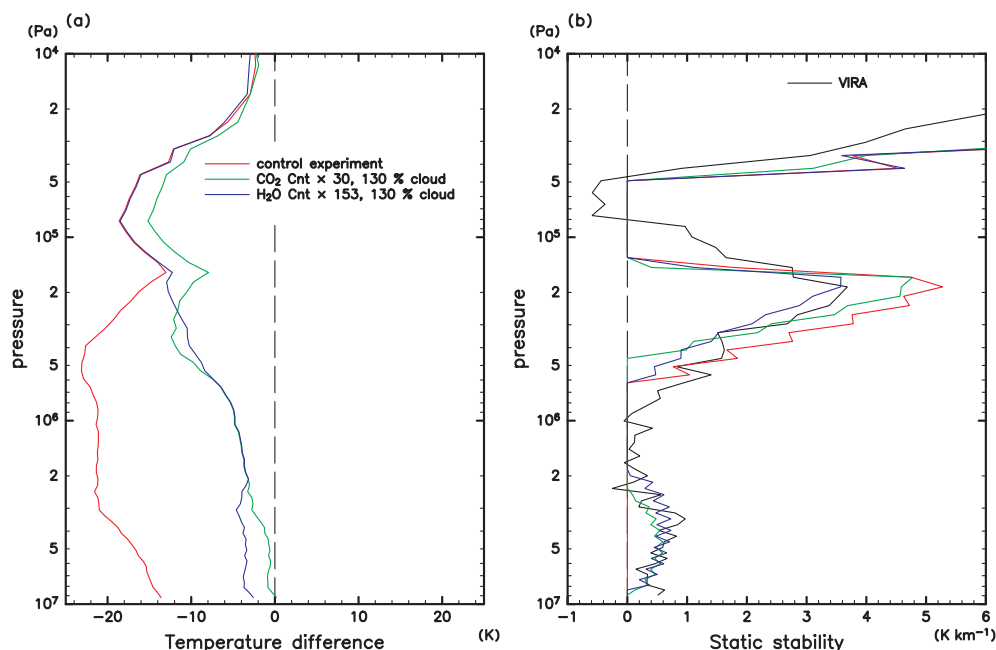


Fig. 10. Same as Fig. 6, but for the cases calculated with tuned coefficients of  $\text{CO}_2$  or  $\text{H}_2\text{O}$  continuum absorption in  $3\text{--}10\text{ }\mu\text{m}$  and with the mixing ratios increased to 130 % for both of the clouds and the UV absorber from the control experiment. The green and blue lines show profiles calculated with  $\text{CO}_2$  and  $\text{H}_2\text{O}$  continuum absorption coefficients increased by factors of 30 and 153, respectively.

method. Figure 10 shows the radiative-convective equilibrium profiles calculated with the  $\text{CO}_2$  continuum absorption coefficient increased by a factor of 30, and the  $\text{H}_2\text{O}$  continuum absorption coefficient increased by a factor of 153 both along with the mixing ratios increased to 130 % for both of the clouds and the UV absorber from the control experiment. In the case with the increased  $\text{CO}_2$  continuum absorption coefficient, the mean static stability between  $4 \times 10^6$  Pa and  $7 \times 10^6$  Pa pressure levels is  $0.50\text{ K km}^{-1}$ , and the surface temperature is 735 K. In the case with the increased  $\text{H}_2\text{O}$  continuum absorption coefficient, those are  $0.51\text{ K km}^{-1}$  and 733 K, respectively. Those values are compared well with  $0.50\text{ K km}^{-1}$  and 735 K, respectively, of the low latitude temperature profile of the VIR model. Since a latitudinal variation of about 30 % in cloud optical depth has been deduced (Haus et al. 2013, 2014), the single scattering albedo dependent on the composition and the size distribution of particles has not been revealed fully, and the cloud optical depth appropriate for the global mean equilibrium calculation is not clear, a multiplication factor on mixing ratios of the clouds and the UV absorber was used as another tunable parameter, here. The temperature profile of the VIR model might be explained by

stronger continuum absorption and the variation in the optical depths of the clouds and the UV absorber.

When the coefficients for  $\text{CO}_2$  and  $\text{H}_2\text{O}$  continuum absorption are increased by factors of 30 and 153, respectively,  $\text{CO}_2$  or  $\text{H}_2\text{O}$  continuum absorption are the dominant opacity source in the spectral range of  $3\text{--}9\text{ }\mu\text{m}$ , and the optical depth at  $5 \times 10^6$  Pa pressure level reaches  $10^4\text{--}10^5$  (Fig. 11). The method used to increase the coefficients for continuum absorption in this study may be too simple. However, this study suggests that the determination of the coefficient of continuum absorption in the condition of the Venus lower atmosphere is one of keys to understand the thermal structure there.

## 6. Conclusions

The formation of the stable layer below about  $2 \times 10^6$  Pa pressure level ( $\sim 20\text{ km}$  altitude) in the atmosphere of Venus has been investigated by the use of the radiative-convective equilibrium model. Calculated radiative temperature tendency spectra indicate that the optical depths of the clouds and the UV absorber at wavelengths of  $0.3\text{--}3\text{ }\mu\text{m}$  and that of gas at wavelengths of  $1\text{--}7\text{ }\mu\text{m}$  play an important role in the formation of the stable layer.

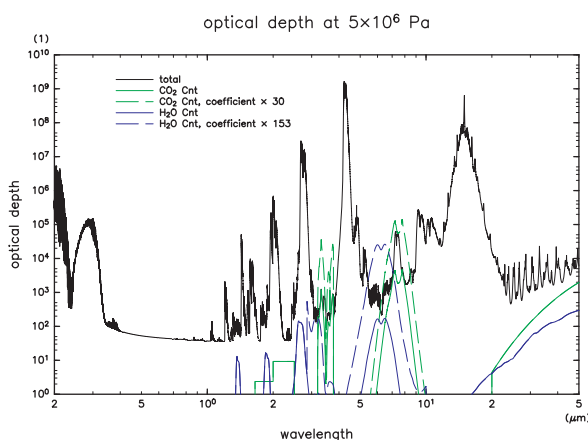


Fig. 11. Spectra of optical depth at  $5 \times 10^6$  Pa pressure level for the low latitude temperature profile of the VIRA model. Solid black, green and blue lines show optical depths of the total extinction, the  $\text{CO}_2$  continuum absorption, and the  $\text{H}_2\text{O}$  continuum absorption, respectively. Dashed green and blue lines show spectra of the  $\text{CO}_2$  and the  $\text{H}_2\text{O}$  continuum absorption with its coefficients increased by factors of 30 and 153 in 3–10  $\mu\text{m}$ , respectively.

Sensitivity experiments have demonstrated that the change in the mixing ratios of the clouds and the UV absorber will not lead to the formation of the stable layer. It has also been indicated that increase in  $\text{H}_2\text{O}$  and  $\text{SO}_2$  mixing ratios and the decrease in CO mixing ratio form the stable layer. However, within the observed range of  $\text{H}_2\text{O}$ ,  $\text{SO}_2$ , and CO mixing ratios, the stability of the formed stable layer is lower than that of the VIRA model. On the other hand, it has been shown that the stable layer forms in the case with the increased coefficient for  $\text{CO}_2$  or  $\text{H}_2\text{O}$  continuum absorption in 3–10  $\mu\text{m}$ . Although the increase in the optical depth of  $\text{CO}_2$  or  $\text{H}_2\text{O}$  continuum absorption raises the surface temperature, the increase in surface temperature can be compensated by an increase in the mixing ratios of the clouds and the UV absorber. When the  $\text{CO}_2$  continuum absorption coefficient is increased by a factor of 30 or the  $\text{H}_2\text{O}$  continuum absorption coefficient is increased by a factor of 153, and the mixing ratios of the clouds and the UV absorber are increased by 30 %, the temperature profile of the radiative-convective equilibrium is close to that of the VIRA model.

Further observations of radiatively active gas in the Venus lower atmosphere and further experimental studies on optical parameters in the condition of the

Venus lower atmosphere are desired to confirm the formation mechanism of the stable layer and to verify the idea on increase in coefficients of continuum absorption performed in this study. On the other hand, this study suggests a practical method to form the stable layer in dynamical models, such as GCMs, of the Venus atmosphere. The studies by the use of the GCMs, which consider spatial variation, are also required to understand both the formation of the stable layer in the lower atmosphere and the observed surface temperature. Further, it would, in turn, provide understanding on the transport and the mixing of the minor constituents and the angular momentum and, as a result, the formation of the superrotation of the Venus atmosphere.

### Data Availability Statement

The data generated and analyzed in this study are available at the JMSJ's J-STAGE Data site, <https://doi.org/10.34474/data.jmsj.25814638>, except for those already published elsewhere. Software developed and used in this study and its newest versions will be available from the web page of GFD Dennou Club, <https://www.gfd-dennou.org/>.

### Acknowledgments

The authors would like to thank Rainer Haus for providing data of optical properties for his cloud model. We are also grateful to two anonymous reviewers for their constructive comments on this article. Visualization software developed by GFD Dennou Club, Dennou Club Library (DCL) and GPhys, are used to make figures shown in this study. A supercomputer of the Education Center on Computational Science and Engineering, Kobe University is used to perform several calculations shown in this study. This study was funded by Grant-in-Aid for Scientific Research on Innovative Areas (JSPS KAKENHI Grant Numbers 17H06457, 19H05605, and 21K03644) from Japan Society for the Promotion of Science.

### Appendix A: Update of the $k$ -distribution table for Venus

A new  $k$ -distribution table is generated to take into account variable  $\text{H}_2\text{O}$ , CO, and  $\text{SO}_2$ . The structure of the new  $k$ -distribution table is the same as those generated for Venus atmosphere by Takahashi et al. (2023), but we added axes of volume mixing ratios of the variable species. In addition, the number of bands and the number of integration points in a band are changed in order to improve the accuracy of the radiative fields in a cloud free condition which was out of scope of

Takahashi et al. (2023). Further, the temperature axis of the table is changed to decrease the amount of computation to generate  $k$ -distribution tables.

The number of bands, the number of integration points, and the intervals of values in volume mixing ratio axes of the  $k$ -distribution table are selected to meet accuracy criterion for the calculated radiative fields. The accuracy criterion is set to  $2 \times 10^{-4} \text{ W m}^{-3}$  for flux convergence following Takahashi et al. (2023). In this study, the criterion is set for solar radiation as well as planetary radiation, though it was set only for planetary radiation by Takahashi et al. (2023). This ensures that radiative fields are calculated with required accuracy in both planetary radiation and solar radiation. To achieve the accuracy criterion, we increased the number of bands to 27. The wavenumber boundaries and number of integration points for the resultant table are shown in Table A1.

The ranges of the volume mixing ratio axes in the table are determined to cover the volume mixing ratios set in this study (Fig. 7). The resultant  $k$ -distribution table has axes of volume mixing ratios as follows: the volume mixing ratio of  $\text{H}_2\text{O}$ ,  $r_{\text{H}_2\text{O}}$ , ranges from  $10^{-7}$  to  $10^{-2}$  with a grid interval of  $\Delta \log_{10} r_{\text{H}_2\text{O}} = 0.5$ , that of  $\text{CO}$ ,  $r_{\text{CO}}$ , ranges from  $10^{-6}$  to  $10^{-4}$  with  $\Delta \log_{10} r_{\text{CO}} = 1$ , and that of  $\text{SO}_2$ ,  $r_{\text{SO}_2}$ , ranges from  $10^{-9}$  to  $10^{-3}$  with  $\Delta \log_{10} r_{\text{SO}_2} = 0.5$ . Volume mixing ratios of species other than  $\text{H}_2\text{O}$ ,  $\text{CO}$ , and  $\text{SO}_2$  are assumed to be fixed based on the profile B of Takahashi et al. (2023), which are based on Pollack et al. (1993).

The temperature axis in the new  $k$ -distribution table has the pressure-dependent temperature of  $T_{\text{VIRA}}(p_i) - 50$ ,  $T_{\text{VIRA}}(p_i)$ ,  $T_{\text{VIRA}}(p_i) + 50 \text{ K}$ , where  $p_i$  is the  $i$ th pressure value, and  $T_{\text{VIRA}}(p_i)$  is the temperature at  $p_i$  of the low latitude temperature profile of the VIRA model. This axis is based on that implemented by Ikeda (2011). By adopting this temperature axis, the amount of computation to generate the  $k$ -distribution table becomes 3/17 of that for the table presented by Takahashi et al. (2023).

Root mean square errors (RMSEs) of  $k$ -distribution calculations in upward (Up) and downward (Dn) fluxes, flux convergences (FlxCnv), and temperature tendencies (Tend) for planetary radiation (PR) and solar radiation (SR) were evaluated by comparing with those by the line-by-line calculations for the low latitude temperature profile of the VIRA model and the radiative-convective equilibrium of the control experiment (Table A2). It is found that the accuracy criterion is met for both profiles in both cloudy and cloud free conditions.

Table A1. The setting for the  $k$ -distribution table generated in this study. IP stands for integration point.

band number	wavenumber range ( $\text{cm}^{-1}$ )	number of IPs in 0–0.98	number of IPs in 0.98–1
1	10– 255	6	1
2	255– 500	6	1
3	500– 600	6	1
4	600– 700	6	1
5	700– 840	6	1
6	840– 980	4	1
7	980– 1185	6	1
8	1185– 1390	4	1
9	1390– 1595	4	1
10	1595– 1800	4	1
11	1800– 2025	4	1
12	2025– 2250	4	1
13	2250– 2750	6	1
14	2750– 3250	6	1
15	3250– 4200	6	4
16	4200– 5150	6	4
17	5150– 6425	6	4
18	6425– 7700	6	4
19	7700–10275	6	4
20	10275–12850	6	4
21	12850–17750	4	1
22	17750–22650	4	1
23	22650–25825	4	1
24	25825–29000	4	1
25	29000–32000	4	1
26	32000–39500	1	1
27	39500–50000	1	1

## Appendix B: Radiative temperature tendency spectrum

The radiative temperature tendency spectrum, Eq. (1), for the radiative-convective equilibrium of the control experiment from the surface up to the top of the model is shown in Fig. B1.

## Appendix C: The cloud model by Haus et al. (2015)

The number density profiles,  $N(z)$ , for the clouds and the UV absorber in the cloud model by Haus et al. (2015) are as follows,

$$N(z) = \begin{cases} N_0 \exp \left\{ -\frac{z - (z_b + z_c)}{H_{up}} \right\} & (z > z_b + z_c), \\ N_0 & (z_b + z_c \geq z \geq z_b), \\ N_0 \exp \left\{ -\frac{z_b + z}{H_{lo}} \right\} & (z < z_b), \end{cases} \quad (\text{C1})$$

Table A2. RMSEs of radiation fluxes ( $\text{W m}^{-2}$ ), their convergences ( $\text{W m}^{-3}$ ), and temperature tendencies ( $\text{K s}^{-1}$ ) calculated from the differences between the corresponding data obtained by the correlated  $k$ -distribution and the line-by-line models at each pressure level for the low latitude temperature profile of the VIRA model and the radiative-convective equilibrium of the control experiment. Up, Dn, PR, SR, FlxCnv, and Tend denote upward flux, downward flux, planetary radiation, solar radiation, flux convergence, and temperature tendency, respectively.

	VIRA		radiative-convective equilibrium	
	cloudy	cloud free	cloudy	cloud free
UpPR	$2.72 \times 10^{-1}$	$8.05 \times 10^{-1}$	$2.20 \times 10^{-1}$	$8.05 \times 10^{-1}$
DnPR	$2.48 \times 10^{-1}$	$4.74 \times 10^{-1}$	$2.12 \times 10^{-1}$	$4.37 \times 10^{-1}$
FlxCnvPR	$6.29 \times 10^{-5}$	$1.55 \times 10^{-4}$	$5.60 \times 10^{-5}$	$1.67 \times 10^{-4}$
TendPR	$1.63 \times 10^{-5}$	$1.63 \times 10^{-5}$	$1.91 \times 10^{-5}$	$1.87 \times 10^{-5}$
UpSR	$2.22 \times 10^{-1}$	$9.19 \times 10^{-1}$	$2.33 \times 10^{-1}$	$9.15 \times 10^{-1}$
DnSR	$3.50 \times 10^{-1}$	$1.98 \times 10^0$	$3.29 \times 10^{-1}$	$1.97 \times 10^0$
FlxCnvSR	$5.33 \times 10^{-5}$	$1.06 \times 10^{-4}$	$5.23 \times 10^{-5}$	$1.09 \times 10^{-4}$
TendSR	$1.68 \times 10^{-5}$	$1.68 \times 10^{-5}$	$1.69 \times 10^{-5}$	$1.69 \times 10^{-5}$

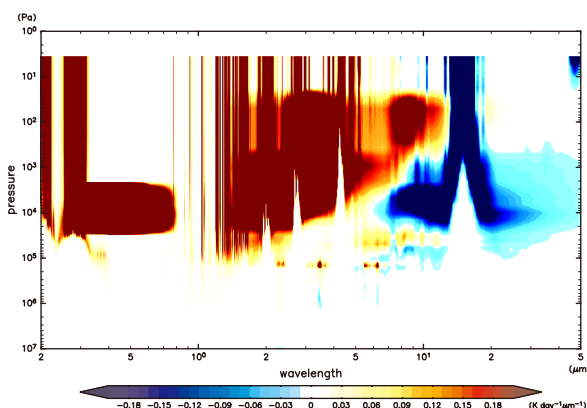


Fig. B1. Same as Fig. 3, but up to the top of the model. It should be noted that the color bar is different from that in Fig. 3.

where  $z$ ,  $z_b$ ,  $z_c$ ,  $H_{up}$ ,  $H_{lo}$ , and  $N_0$  are altitude, the lower base of peak altitude, the layer thickness of constant peak particle number density, the upper scale height, the lower scale height, and the peak number density, respectively. The parameters used for the experiment in Section 4.1 is shown in Table C1.

Refractive index data for a  $\text{H}_2\text{SO}_4$  solution of 75 % by weight described by Haus et al. (2015) are used to calculate extinction efficiency factor, single scattering albedo, and asymmetry factor of the cloud particles.

## References

- Allen, D. A., and J. W. Crawford, 1984: Cloud structure on the dark side of Venus. *Nature*, **307**, 222–224.
- Avdujevskiy, V. S., M. Y. Marov, Y. N. Kulikov, V. P. Shari, A. Y. Gorbachevskiy, G. R. Uspenskiy, and Z. P. Cheremukhina, 1983: Structure and parameters of the Venus atmosphere according to Venera probe data. *Venus*. Hunt, D. M., L. Colin, T. M. Donahue, and V. I. Moroz (eds.), The University of Arizona Press, 280–298.

Table C1. Values of the parameters used in the number density formulation given by Eq. (C1) for the clouds and the UV absorber.

	$z_b$ (km)	$z_c$ (km)	$H_{up}$ (km)	$H_{lo}$ (km)	$N_0$ ( $\text{cm}^{-3}$ )
mode 1	49.0	16.0	3.5	1.0	96.75
mode 2	62.0	1.0	1.0	3.0	50.00
mode 2'	49.0	11.0	1.0	0.1	100.00
mode 3	49.0	8.0	1.0	0.5	28.00
UV absorber	58.0	12.0	1.0	1.0	10.00



- Baker, R. D., G. Schubert, and P. W. Jones, 2000a: Convectively generated internal gravity waves in the lower atmosphere of Venus. Part I: No wind shear. *J. Atmos. Sci.*, **57**, 184–199.
- Baker, R. D., G. Schubert, and P. W. Jones, 2000b: Convectively generated internal gravity waves in the lower atmosphere of Venus. Part II: Mean wind shear and wave-mean flow interaction. *J. Atmos. Sci.*, **57**, 200–215.
- Bertaux, J.-L., T. Widemann, A. Hauchecorne, V. I. Moroz, and A. P. Ekonomov, 1996: VEGA 1 and VEGA 2 entry probes: An investigation of local UV absorption (220–400 nm) in the atmosphere of Venus (SO<sub>2</sub>, aerosols, cloud structure). *J. Geophys. Res.*, **101**, 12709–12745.
- Bézar, B., C. de Bergh, D. Crisp, and J.-P. Maillard, 1990: The deep atmosphere of Venus revealed by high-resolution nightside spectra. *Nature*, **345**, 508–511.
- Bézar, B., C. de Bergh, B. Fegley, J.-P. Maillard, D. Crisp, T. Owen, J. B. Pollack, and D. Grinspoon, 1993: The abundance of sulfur dioxide below the clouds of Venus. *Geophys. Res. Lett.*, **20**, 1587–1590.
- Connes, P., J. Connes, L. D. Kaplan, and W. S. Benedict, 1968: Carbon monoxide in the Venus atmosphere. *Astrophys. J.*, **152**, 731–743.
- Crisp, D., 1986: Radiative forcing of the Venus mesosphere: I. Solar fluxes and heating rates. *Icarus*, **67**, 484–514.
- Crisp, D., 1989: Radiative forcing of the Venus mesosphere: II. Thermal fluxes, cooling rates, and radiative equilibrium temperatures. *Icarus*, **77**, 391–413.
- de Bergh, C., B. Bézar, D. Crisp, J. P. Maillard, T. Owen, J. Pollack, and D. Grinspoon, 1995: Water in the deep atmosphere of Venus from high-resolution spectra of the nightside. *Adv. Space Res.*, **15**, 79–88.
- Esposito, L. W., R. G. Knollenberg, M. Y. Marov, O. B. Toon, and R. P. Turco, 1983: The clouds and hazes of Venus. *Venus*. Hunten, D. M., L. Colin, T. M. Donahue, and V. I. Moroz (eds.), The University of Arizona Press, 484–564.
- Eymet, V., R. Fournier, J.-L. Dufresne, S. Lebonnois, F. Hourdin, and M. A. Bullock, 2009: Net exchange parameterization of thermal infrared radiative transfer in Venus' atmosphere. *J. Geophys. Res.*, **114**, E11008, doi:10.1029/2008JE003276.
- Gel'man, B. G., V. G. Zolotukhin, N. I. Lamonov, B. V. Levchuk, L. M. Mukhin, D. F. Nenarokov, B. P. Khotnikov, V. A. Rotin, and A. N. Lipatov, 1979: An analysis of the chemical composition of the atmosphere of Venus on an AMS of the Venera-12 using a gas chromatograph. (Translated from the Russian: "Analiz Khimicheskogo Sostava Atmosfery Venery na AMS Venera-12 Gazovym Khromatografom" (Moscow). *Technical Memorandum*, NASA/TM -75476, NASA, 13 pp. [Available at <https://ntrs.nasa.gov/api/citations/19790017793/downloads/19790017793.pdf>.]
- Gernert, J., and R. Span, 2016: EOS-CG: A Helmholtz energy mixture model for humid gases and CCS mixtures. *J. Chem. Thermodynamics*, **93**, 274–293.
- Hashimoto, G. L., M. Roos-Serote, S. Sugita, M. S. Gilmore, L. W. Kamp, R. W. Carlson, and K. H. Baines, 2008: Felsic highland crust on Venus suggested by Galileo near-infrared mapping spectrometer data. *J. Geophys. Res.*, **113**, E00B24, doi:10.1029/2008JE003134.
- Haus, R., D. Kappel, and G. Arnold, 2013: Self-consistent retrieval of temperature profiles and cloud structure in the northern hemisphere of Venus using VIRTIS/VEX and PMV/VENERA-15 radiation measurements. *Planet. Space Sci.*, **89**, 77–101.
- Haus, R., D. Kappel, and G. Arnold, 2014: Atmospheric thermal structure and cloud features in the southern hemisphere of Venus as retrieved from VIRTIS/VEX radiation measurements. *Icarus*, **232**, 232–248.
- Haus, R., D. Kappel, and G. Arnold, 2015: Radiative heating and cooling in the middle and lower atmosphere of Venus and responses to atmospheric and spectroscopic parameter variations. *Planet. Space Sci.*, **117**, 262–294.
- Hoffman, J. H., R. R. Hodges, T. M. Donahue, and M. B. McElroy, 1980a: Composition of the Venus lower atmosphere from the Pioneer Venus mass spectrometer. *J. Geophys. Res.*, **85**, 7882–7890.
- Hoffman, J. H., R. R. Hodges, W. W. Wright, V. A. Blevins, K. D. Duerksen, and L. D. Brooks, 1980b: Pioneer Venus sounder probe neutral gas mass spectrometer. *IEEE Trans. Geosci. Remote Sens.*, **18**, 80–84.
- Ikeda, K., 2011: *Development of radiative transfer model for Venus atmosphere and simulation of superrotation using a general circulation model*. PhD thesis, The University of Tokyo.
- Johnson, N. M., and M. R. R. de Oliveira, 2019: Venus atmospheric composition in situ data: A compilation. *Earth Space Sci.*, **6**, 1299–1318.
- Lebonnois, S., and G. Schubert, 2017: The deep atmosphere of Venus and the possible role of density-driven separation of CO<sub>2</sub> and N<sub>2</sub>. *Nat. Geosci.*, **10**, 473–477.
- Lebonnois, S., V. Eymet, C. Lee, and J. V. d'Ollone, 2015: Analysis of the radiative budget of the Venusian atmosphere based on infrared Net Exchange Rate formalism. *J. Geophys. Res.: Planets*, **120**, 1186–1200.
- Lebonnois, S., N. Sugimoto, and G. Gilli, 2016: Wave analysis in the atmosphere of Venus below 100-km altitude, simulated by the LMD Venus GCM. *Icarus*, **278**, 38–51.
- Lebonnois, S., G. Schubert, F. Forget, and A. Spiga, 2018: Planetary boundary layer and slope winds on Venus. *Icarus*, **314**, 149–158.
- Lee, C., and M. I. Richardson, 2011: A discrete ordinate, multiple scattering, radiative transfer model of the Venus atmosphere from 0.1 to 260  $\mu\text{m}$ . *J. Atmos. Sci.*, **68**, 1323–1339.
- Marq, E., B. Bézar, P. Drossart, G. Piccioni, J. M. Reess, and F. Henry, 2008: A latitudinal survey of CO, OCS,

- H<sub>2</sub>O, and SO<sub>2</sub> in the lower atmosphere of Venus: Spectroscopic studies using VIRTIS-H. *J. Geophys. Res.*, **113**, E00B07, doi:10.1029/2008JE003074.
- Marov, M. Y., V. P. Volkov, Y. A. Surkov, and M. L. Ryvkin, 1989: The lower atmosphere. *The Planet Venus: Atmosphere, Surface, Interior Structure*. Barsukov, V. L., and V. P. Volkov (eds.), Nauka, 25–67 (in Russian).
- Matsuda, Y., and T. Matsuno, 1978: Radiative-convective equilibrium of the Venusian atmosphere. *J. Meteor. Soc. Japan*, **56**, 1–18.
- Meador, W. E., and W. R. Weaver, 1980: Two-stream approximations to radiative transfer in planetary atmospheres: A unified description of existing methods and a new improvement. *J. Atmos. Sci.*, **37**, 630–643.
- Mendonça, J. M., P. L. Read, C. F. Wilson, and C. Lee, 2015: A new, fast and flexible radiative transfer method for Venus general circulation models. *Planet. Space Sci.*, **105**, 80–93.
- Mlawer, E. J., V. H. Payne, J.-L. Moncet, J. S. Delamere, M. J. Alvarado, and D. C. Tobin, 2012: Development and recent evaluation of the MT\_CKD model of continuum absorption. *Philos. Trans. Roy. Soc. London, Ser. A*, **370**, 2520–2556.
- Moroz, V. I., N. A. Parfentev, and N. F. Sanko, 1979: Spectrophotometric experiment on the Venera 11 and Venera 12 descent modules. II - Analysis of Venera 11 spectra data by the layer-addition method. *Cosmic Res.*, **17**, 601–614.
- Oyama, K. I., G. C. Carle, J. B. Woeller, J. B. Pollack, R. T. Reynolds, and R. A. Craig, 1980: Pioneer Venus gas chromatography of the lower atmosphere of Venus. *J. Geophys. Res.*, **85**, 7891–7902.
- Pollack, J. B., and R. Young, 1975: Calculations of the radiative and dynamical state of the Venus atmosphere. *J. Atmos. Sci.*, **32**, 1025–1037.
- Pollack, J. B., J. B. Dalton, D. Grinspoon, R. B. Wattson, R. Freedman, D. Crisp, D. A. Allen, B. Bézard, C. DeBergh, L. P. Giver, Q. Ma, and R. Tipping, 1993: Near-infrared light from Venus' nightside: A spectroscopic analysis. *Icarus*, **103**, 1–42.
- Ragent, B., L. W. Esposito, M. G. Tomasko, M. Y. Marov, V. P. Shari, and V. N. Lebedev, 1985: Particulate matter in the Venus atmosphere. *Adv. Space Res.*, **5**, 85–115.
- Seiff, A., 1983: Thermal structure of the atmosphere of Venus. *Venus*. Hunten, D. M., L. Colin, T. M. Donahue, and V. I. Moroz (eds.), The University of Arizona Press, 215–279.
- Seiff, A., and the VEGA Balloon Science Team, 1987: Further information on structure of the atmosphere of Venus derived from the VEGA Venus balloon and lander mission. *Adv. Space Res.*, **7**, 323–328.
- Seiff, A., D. B. Kirk, R. E. Young, R. C. Blanchard, J. T. Findlay, G. M. Kelly, and S. C. Sommer, 1980: Measurements of thermal structure and thermal contrasts in the atmosphere of Venus and related dynamical observations: Results from the four Pioneer Venus probes. *J. Geophys. Res.*, **85**, 7903–7933.
- Seiff, A., J. T. Schofield, A. J. Kliore, F. W. Taylor, S. S. Limaye, H. E. Revercomb, L. A. Sromovsky, V. V. Kerzhanovich, V. I. Moroz, and M. Y. Marov, 1985: Models of the structure of the atmosphere of Venus from the surface to 100 kilometers altitude. *Adv. Space Res.*, **5**, 3–58.
- Sugimoto, N., M. Takagi, and Y. Matsuda, 2019: Fully developed superrotation driven by the mean meridional circulation in a Venus GCM. *Geophys. Res. Lett.*, **46**, 1121–1188.
- Takagi, M., K. Suzuki, H. Sagawa, P. Baron, J. Mendrok, Y. Kasai, and Y. Matsuda, 2010: Influence of CO<sub>2</sub> line profiles on radiative and radiative-convective equilibrium states of the Venus lower atmosphere. *J. Geophys. Res.*, **115**, E06014, doi:10.1029/2009JE003488.
- Takahashi, Y. O., Y.-Y. Hayashi, G. L. Hashimoto, K. Kuramoto, and M. Ishiwatari, 2023: Development of a line-by-line and a correlated *k*-distribution radiation models for planetary atmospheres. *J. Meteor. Soc. Japan*, **101**, 39–66.
- Takahashi, Y. O., Y.-Y. Hayashi, G. L. Hashimoto, K. Kuramoto, M. Ishiwatari, and H. Kashimura, 2024: Dependence of the radiative convective equilibrium structure of the lower atmosphere of Venus on the thermodynamic model. *J. Meteor. Soc. Japan*, **102**, 5–16.
- Taylor, F. W., D. Crisp, and B. Bézard, 1997: Near-infrared sounding of the lower atmosphere of Venus. *Venus II*. Bougher, S. W., D. M. Hunten, and R. Phillips (eds.), The University of Arizona Press, 325–351.
- Titov, D. V., M. A. Bullock, D. Crisp, N. O. Renno, F. W. Taylor, and L. V. Zasova, 2007: Radiation in the atmosphere of Venus. *Exploring Venus as a Terrestrial Planet*. Esposito, L. W., E. R. Stofan, and T. E. Cravens (eds.), Wiley, 121–138.
- Toon, O. B., C. P. McKay, T. P. Ackerman, and K. Santhanam, 1989: Rapid calculation of radiative heating rates and photodissociation rates in inhomogeneous multiple scattering atmospheres. *J. Geophys. Res.*, **94**, 16287–16301.
- Tsang, C. C. C., F. W. Taylor, C. F. Wilson, S. J. Liddell, P. G. J. Irwin, G. Piccioni, P. Drossart, and S. B. Calcutt, 2009: Variability of CO concentrations in the Venus troposphere from Venus Express/VIRTIS using a Band Ratio Technique. *Icarus*, **201**, 432–443.
- von Zahn, U., S. Kumar, H. Niemann, and R. Prinn, 1983: Composition of the Venus atmosphere. *Venus*. Hunten, D. M., L. Colin, T. M. Donahue, and V. I. Moroz (eds.), The University of Arizona Press, 299–430.
- Winick, J. R., and A. I. F. Stewart, 1980: Photochemistry of SO<sub>2</sub> in Venus' upper cloud layers. *J. Geophys. Res.*, **85**, 7849–7860.
- Young, L. D. G., 1972: High-resolution spectra of Venus: A review. *Icarus*, **17**, 632–658.